To appear, Journal of Micromechatronics
VSP International Science Publishing
2002

Wing Transmission for a Micromechanical Flying Insect *†

J. Yan[1], S.A. Avadhanula[2], J. Birch[3], M.H. Dickinson[3],
M. Sitti[1], T. Su[4], and R.S. Fearing[1]
(1) Electrical Engineering and Computer Sciences
(2) Mechanical Engineering (3) Integrative Biology
(4) Materials Science & Engineering
University of California
Berkeley, CA 94720-1770

Abstract

Flapping wings provide unmatched maneuverability for flying micro-robots. Recent advances in modelling insect aerodynanamics show that adequate wing rotation at the end of the stroke is essential for generating adequate flight forces. A thorax structure has been developed utilizing planar 4-bar frames combined with a spherical 5-bar differential to provide adequate wing stroke and rotation. Calculations using a simple resonant mechanical circuit model show that piezoelectric actuators generate sufficient power, force and stroke to drive the wings at 150 Hz.

1 Introduction

The micromechanical flying insect (MFI) project entails the development of a centimeter-scale robot capable of flying using flapping wings. Commercial and military applications for micro aerial vehicles such as this have been identified including operations in hazardous environments (*e.g.,* search-and-rescue within collapsed buildings, nuclear plant exploration during a radiation leak, *etc.*) and defense-related missions (*e.g.,* reconnaissance and surveillance).

Flapping flight for micro-robots is not only an intriguing mode of locomotion, but provides maneuverability not achievable with fixed or rotary wing aircraft. Biological insects can fly with a payload equal to their body mass and have peak accelerations approaching $10m/s^2$ [14]. Although they require relatively still air, flying micro-robots could fly over terrain which would be impassable for a legged micro-robot. Following the initial vision of Flynn [7], pioneering work in micro-robotic flight was started by Shimoyama (see [20], [12], and [16]) and more recently, milli-robotic flapping flight by Cox *et al* [2]. Previous work on the MFI has been documented in several areas by Fearing *et al* [6], Yan *et al* [25], Sitti *et al* [21] and Schenato *et al* [18].

This paper considers the kinematic and power requirements for the MFI and presents the current thorax design for the device. The design, shown in Figure 1, utilizes planar

*This paper is an expanded version of Fearing *et al* [6].

†This work was funded by ONR MURI N00014-98-1-0671 and DARPA.

flexural 4-bar elements to amplify small piezoelectric actuator displacements and a 5-bar spherical differential mechanism to map the motions into flapping and rotational movements.

The design target for the MFI is the blowfly Calliphora, which has a mass of $100mg$, wing length of $11mm$, wing beat frequency of $150Hz$, and actuator power of roughly $8mW$. At this size scale, the current best understanding of non-steady state aerodynamics comes from experimental observations of real insects and kinematically similar mockups, most notably, work by Ellington *et al* [5] and by Dickinson *et al* [3].

Figure 1(a) illustrates the proposed components of the MFI. A photo of a mock-up, fabricated to scale (but without actuation), is shown in Figure 1(c). Table 1 summarizes the size and mass specifications of some MFI thorax components.

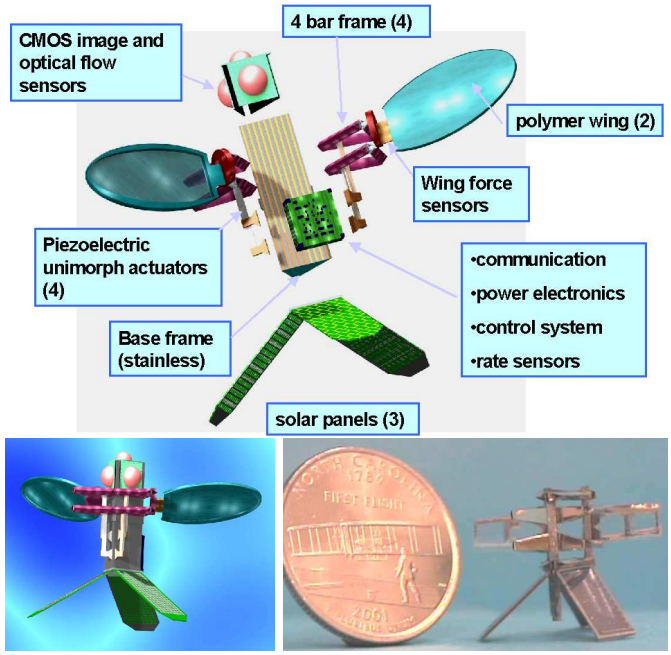

Figure 1: (a) Pre-assembled view showing modular components; (b) Conceptual rendition of MFI; and (c) Structural mock-up at final scale.

MFI component	size	total mass
4-bar frames (2 per wing)	links 5, 5, 5, 1 mm	22 mg
skeletal airframe (triangular prism)	6 mm equilateral triangle × 10 mm long	24 mg
piezo actuator (2 per wing)	$5 \times 1.1 \times 0.13$ mm^3	20 mg
wings	$4 \times 10 \times .007$ mm^3	1 mg
total structure		67 mg

Table 1: Thorax components of the MFI. The frames are folded from $12.5\mu m$ stainless steel shim. Flexures are cut from $6.25\mu m$ polyester sheets and wings are made from polyimide spincoated down to $7\mu m$.

2 Insect Unsteady Aerodynamics

It has long been known that insect flight cannot be explained by steady state aerodynamics and only in recent years has there been elucidation of the unsteady aerodynamic mechanisms which account for the large lift forces generated. Francis and Cohen appear to have been the first to study impulsive wing translational motions which give rise to the phenomenon known as *delayed stall* [8]; this effect has recently been quantified using a scaled model of a hawkmoth by Ellington *et al* [5]. Dickinson *et al* observed that this phenomenon was inadequate in accounting for the total lift and, using Robofly, established two additional important lift mechanisms: *rotational lift* and *wake capture* [4].

RoboFly, shown in Figure 2, is a dynamically-scaled model of Drosophila (the fruitfly). It consists of two wings, each driven by 3 stepping motors, which can closely mimic the stroke kinematics of Drosophila or follow other arbitrary trajectories. Strain gauges measure instantaneous wing forces and the integral of forces around a closed wing beat cycle can be measured to determine net flight forces. Robofly running with a wing beat frequency of $1/6Hz$ in mineral oil has the same Reynold's number as a fruitfly with wing beat frequency $220Hz$ in air. By pumping air bubbles into the oil tank, digital particle image velocimetry (DPIV) can be used for flow visualization.

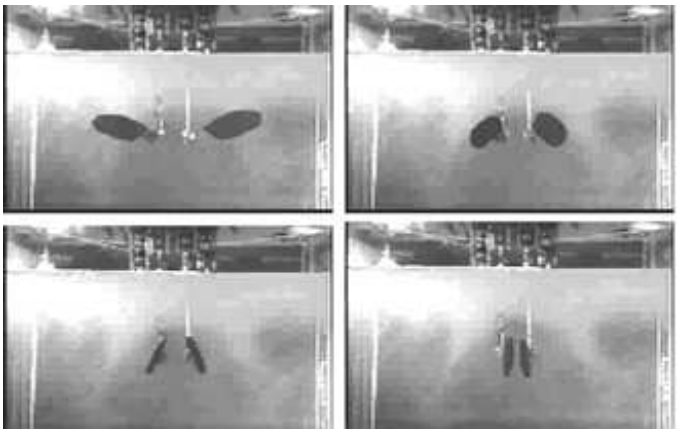

Figure 2: Robofly apparatus in mineral oil tank.

Dickinson *et al* have found wing trajectories which generate peak lift forces of four times the equivalent insect weight [4]. At the bottom of a stroke, the wing rotates resulting in the *rotational lift* forces. The timing of this rotation can change the net lift from positive to negative, as seen in Figure 3. The second key finding was the significant force generated by *wake capture* at the top and bottom of the stroke when the wings recover some of the kinetic energy imparted to the air in the previous stroke. These results are directly relevant to the wing kinematics of the MFI, as it appears that a rapid wing rotation of 90° needs to occur before the end of the down stroke to create adequate lift. These three stroke components of force generation can be seen in the flow patterns created by Robofly using DPIV (see Figure 4). These panels begin with the wing moving toward the left, rotating, and reversing direction. The first panel shows the typical flow and forces during translation. At mid rotation (panel 0.46) there is a peak in total force, although mostly directed in the rearward (drag) direction. Wake capture is evident at 0.59 of the stroke cycle, where the total force peak is greatest and corresponds to the peak forces seen for advanced rotation in Figure 3

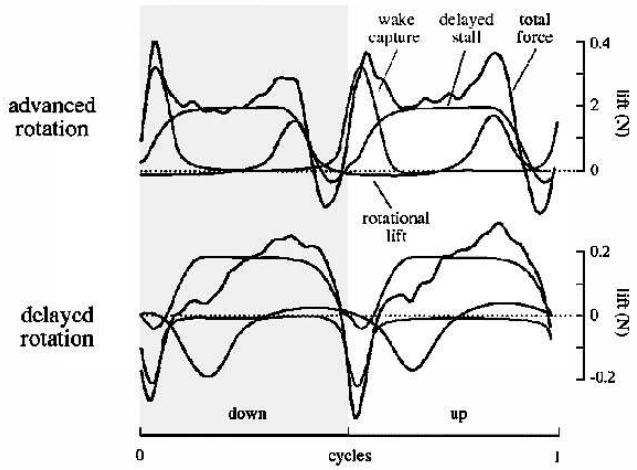

Figure 3: Experimental data from Robofly. The timing of wing rotation has a major effect on net lift. Advanced rotation, before the end of the stroke, significantly increases lift. (Adapted from Dickinson *et al* [4])

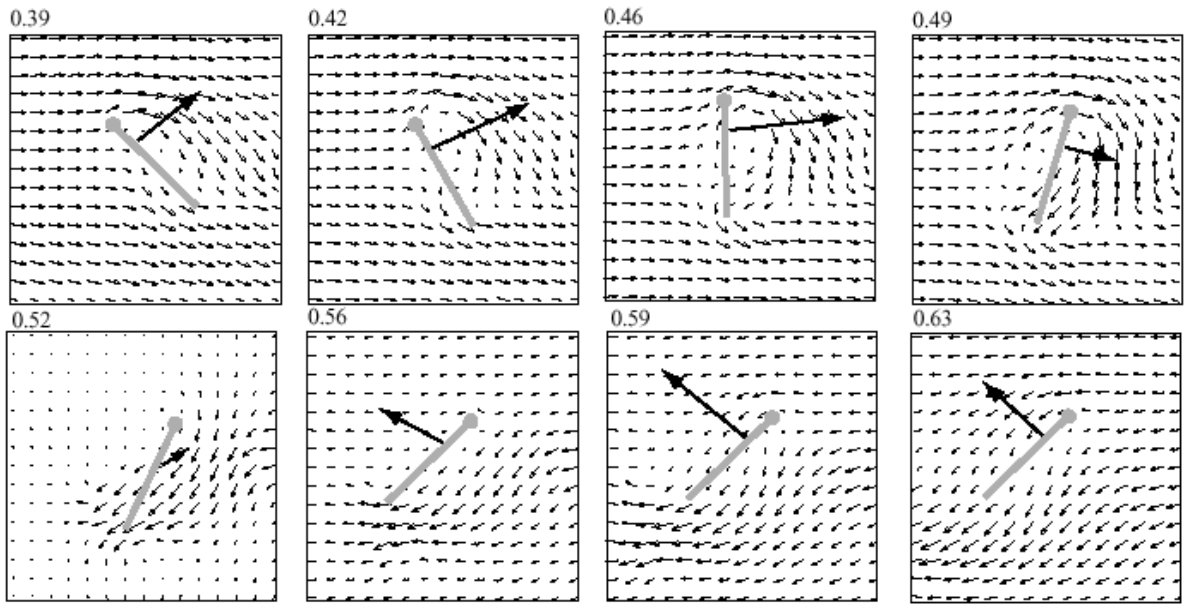

Figure 4: Robofly flow visualization during translation, rotation, and wake capture with images captured at 0.65R (R=wing length). The gray bar shows the wing chord, the circle represents the leading edge and the large arrow indicates the instantaneous force vector. Fluid flow is shown relative to wing motion so that the wing appears to be stationary in the sequence (in the first panel, the wing is actually moving towards the left). The panel numbers indicate the proportion of the complete stroke cycle.

3 Thorax and Wing Design

Insect flight at the centimeter scale requires both large stroke amplitude and wing rotation [4]. Drosophila uses a wing stroke of 160° combined with wing rotation of over 90°. The thorax of a biological insect uses a complicated arrangement of linkages and cams [17] which is not fully understood and is too difficult to fabricate. For each wing, the MFI thorax design, illustrated in Figure 5, uses a pair of 4-bar frames to control two links of

a spherical 5-bar mechanism, permitting the necessary 2 degrees of freedom (DOF).

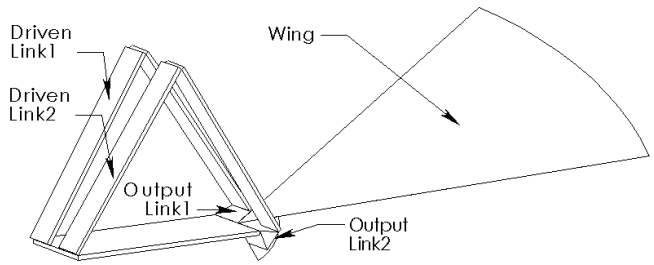

Figure 5: Assembly of the planar 4-bar pair with a spherical 5-bar permits wing flapping and rotation.

3.1 Planar 4-Bar Kinematic Analysis

Figure 6(a) shows a 1 DOF planar 4-bar mechanism with link 1 fixed. The output link angle θ_4 is a function of the driven link angle θ_2:

$$\theta_4 = 180^\circ - (\delta_1 + \delta_2) \tag{1}$$

where

$$\begin{aligned} z &= (l_1^2 + l_2^2 - 2l_1 l_2 \cos\ \theta_2)^{\frac{1}{2}} \\ \delta_1 &= \cos^{-1}\left(\frac{z^2 + l_1^2 - l_2^2}{2zl_1}\right) \\ \delta_2 &= \pm\cos^{-1}\left(\frac{z^2 + l_4^2 - l_3^2}{2zl_4}\right) \end{aligned} \tag{2}$$

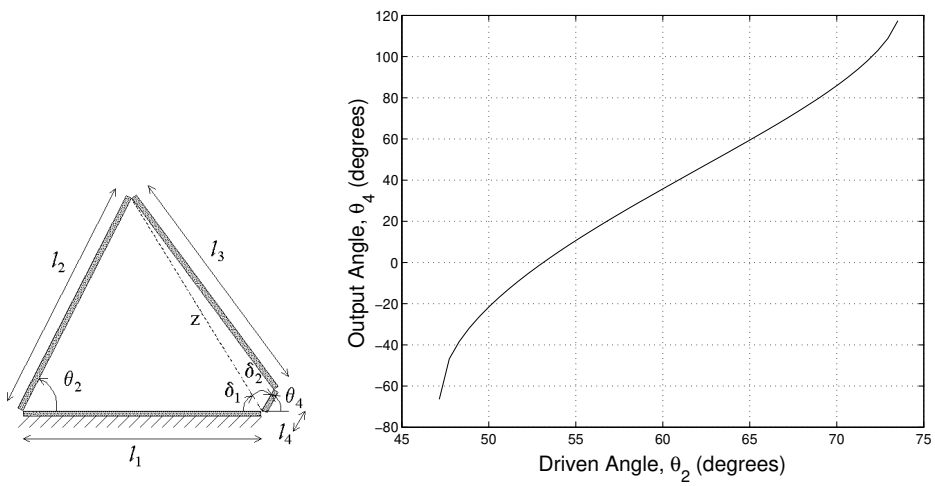

Figure 6: (a) Planar 4-bar kinematics and (b) input/output characteristics with link lengths $l_1 = l_2 = l_3 = 5mm$ and $l_4 = 1mm$.

δ_2 can take on two different values, corresponding to two valid 4-bar configurations. For a given initial configuration, the forward kinematics can uniquely be determined if singularities are avoided. The angular motion range for the driven link can be found

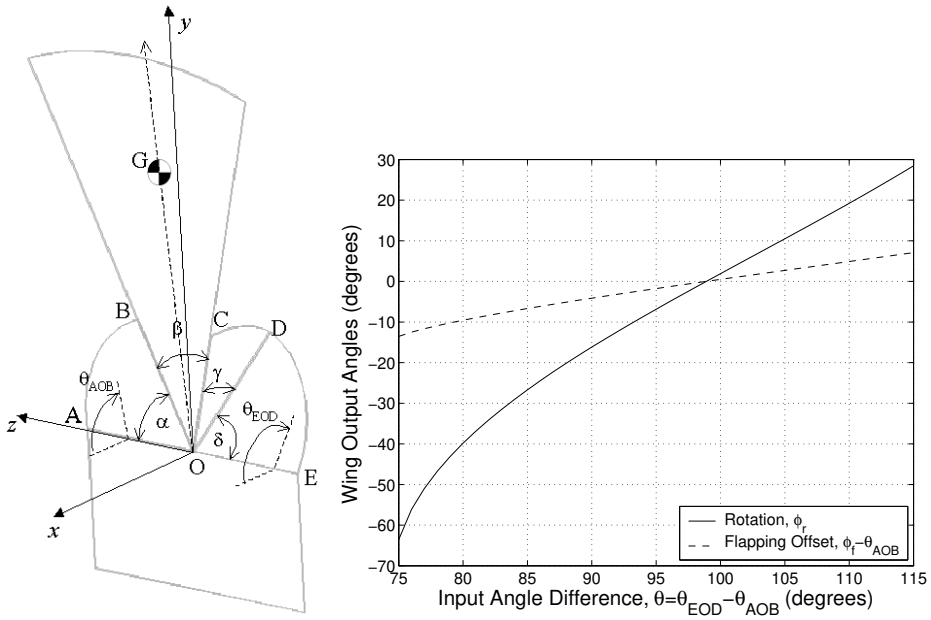

Figure 7: (a) Spherical 5-bar kinematics and (b) Input/Output characteristics with $\alpha = \gamma = \delta = 75°$ and $\beta = 30°$.

by observing that the minimum angle corresponds to $z = l_3 - l_4$ (easily seen by setting $\delta_2 = 180°$) while the maximum angle corresponds to $z = l_3 + l_4$ (or $\delta_2 = 0°$). The corresponding range for θ_2 can be found by using equation (2).

For link lengths $l_1 = l_2 = l_3 = 5mm$ and $l_4 = 1mm$, the 4-bar input/output characteristics are shown in Figure 6(b). The driven link moves beween 47° and 74° (a range of 27°) to provide output motion between $-66°$ and 117° (a range of 173°). Thus, the angular motion magnification is 6.4 when operating over the entire range although the value is much closer to 5 near the nominal operating point. This magnification allows a piezoelectric unimorph with small angle deflection to be used as the actuator as described in Section 4.

3.2 Spherical 5-Bar Kinematic Analysis

The kinematics of the spherical 5-bar differential shown in Figure 7(a) will now be analyzed. Consider the vectors **A, B, C, D, E** to be on the unit sphere centered about the origin **O**. The link vertex angles are α, β, γ and δ (such that $\cos\alpha = \mathbf{A} \cdot \mathbf{B}$, *etc.*). The planar links **AOB** and **EOD** are rigidly attached to the output links of the 4-bars and are driven about the z-axis by angles $\theta_{\mathbf{AOB}}$ and $\theta_{\mathbf{EOD}}$ with respect to the x-z plane, as shown. By construction, constant offsets will exist between these angles and the 4-bar output angles (*i.e.*, $\theta_{\mathbf{AOB}} = \theta_{4,lag} + \Delta\theta_{4,lag}$ and $\theta_{\mathbf{EOD}} = \theta_{4,lead} + \Delta\theta_{4,lead}$, where the subscripts *lead* and *lag* refer to the 4-bar frames associated more directly with the wing leading edge and the wing lagging edge, respectively).

Initially, fix $\theta_{\mathbf{AOB}}$ so that **B** is fixed and the mechanism is reduced to a spherical 4-bar (the kinematic analysis for this can be found in a standard text on linkages and mechanisms such as [15] by McCarthy). The vertex angle of the new "fixed" link of this 4-bar is given by $\zeta = \cos^{-1}(\mathbf{B} \cdot \mathbf{E})$. Let the difference between the driven link angles be given by θ:

$$\theta = \theta_{\mathbf{EOD}} - \theta_{\mathbf{AOB}} \tag{3}$$

Next, define new functions $\mu(\theta)$, $\nu(\theta)$, and $\xi(\theta)$:

$$\begin{aligned}\mu(\theta) &= -\sin\beta(\cos\theta\sin\delta\cos\zeta + \cos\delta\sin\zeta)\\ \nu(\theta) &= \sin\theta\sin\delta\sin\beta\\ \xi(\theta) &= \cos\gamma + \cos\beta(\cos\theta\sin\delta\sin\zeta - \cos\delta\cos\zeta)\end{aligned} \tag{4}$$

The wing rotation angle ϕ_r is naturally defined as the angle made between planes **AOB** and **BOC** and can be calculated as:

$$\phi_r(\theta) = \tan^{-1}\frac{\nu(\theta)}{\mu(\theta)} \pm \cos^{-1}\frac{\xi(\theta)}{\sqrt{\mu^2(\theta)+\nu^2(\theta)}} \tag{5}$$

As with the 4-bar, there are two solutions for this wing rotation but it can also be uniquely determined if the initial configuration is known and singularities are avoided.

The flapping angle ϕ_f is not so naturally defined and several candidates come to mind. For example, the flapping angle may reasonably be based on motion of the wing leading edge, the center of area, the wing angular bisector, or the intersection between the wing and the stroke plane. Each of these choices provides different flapping values for a specific configuration. One alternative which would allow for a simple calculation is to define ϕ_r as the average of the driven link angles (*i.e.*, $\phi_f = (\theta_{\mathbf{AOB}} + \theta_{\mathbf{EOD}})/2$); this option suffers from the problem that the calculated flapping angle, in general, may not geometrically correspond well to the flapping angle of the physical wing.

In this paper, the choice of the flapping angle is based on the motion of the wing center of area **G**. Consider a flat plate with one edge hinged to the z-axis. If this plate is rotated so that it coincides with **G**, then ϕ_f will be the angle made between the plate and the $+x$-axis. This can be found by projecting **G** onto the x-y plane and finding the angle that this projected vector makes with the x-axis.

For a wing differential with physical parameters $\alpha = \gamma = \delta = 75°$ and $\beta = 30°$, the output wing rotation and flapping angle characteristics are shown in Figure 7(b). Wing rotation over 90° can be achieved by changing θ over a range of 40°. Notice that ϕ_f depends on θ but is offset by $\theta_{\mathbf{AOB}}$ so that only $\phi_f - \theta_{\mathbf{AOB}}$ needs to be plotted. For limited input angle ranges for $\theta_{\mathbf{AOB}}$ and $\theta_{\mathbf{EOD}}$, the ranges for ϕ_r and ϕ_f are coupled and one may be increased at the expense of the other. If the input angle range is 173° and ϕ_r must have a range of 90°, then the maximum flapping range is, optimistically, 153° (this necessitates nearing singularities for both the 4-bars and the wing differential so a range for ϕ_f of 140° is much more realistic and attainable). It should also be observed that $\phi_r = 0°$ near $\theta = 98°$ and this difference would be built into the structure (*e.g.*, $\Delta\theta_{4,lead} - \Delta\theta_{4,lag} = 98°$).

3.3 Thorax and Wing Construction

Thorax construction materials should be chosen for high stress limits, high endurance, and low loss (Table 3.3). The thorax of a biological insect is grown from cuticle with resilin connections (see Jensen and Weis-Fogh [10]), which compares very well in stress limitations with stainless steel. Polysilicon is a good structural material, but is more difficult to handle and process than stainless steel. Note that peak stress must be limited to maintain life. This can be done with thin materials, and by keeping the overall system Q low since high Q increases dynamic stresses. While the overall Q of the actuator-wing system is predicted to be only ≈ 2.5 (Section 4) due to wing and actuator dissipation, for

property	polysilicon	302 stainless	polyester	polyimide	cuticle	resilin
Elastic modulus, E (GPa)	140	181	3.6	2.4	10	0.002
Yield stress (MPa)	700	1000	55	128	400	
Ultimate extension	2%	0.5%	124%	10%	2-3%	300%
Endurance limit (GPa)	0.7	0.5				
$(> 10^6$ cycles)	0.5%	0.3%	?	?	?	?
Q = π/lossfactor	10^4	1000	70	500	30	> 100
Density (mg/mm^3)	2.3	7.9	1.4	1.4	1.3	?
Wave velocity $\sqrt{E/\rho}$ (m/s)	7800	5000	1600	1300	2800	?

Table 2: Comparison of properties for possible materials for thorax and wing. Properties are extracted from [11] for polysilicon, www.matls.com for stainless steel and polyester, www.hdmicrosystems.com for polyimide and [10] for cuticle and resilin.

reasonable efficiency, the internal dissipation of the structural material should be kept low [9].

The 4-bar frames need to have a very high strength-to-weight ratio and this is achieved using hollow beams which can be several orders of magnitude stiffer than a solid beam of the same mass (as pointed out by Yeh *et al* [26]). Solid rectangular and triangular beams of width w and height h have respective cross-sectional moments of inertia [1]:

$$I_{rect} = wh^3/12 \quad \text{and} \quad I_{tri} = wh^3/36 \ . \tag{6}$$

The stiffness of a cantilever beam of length l and modulus E in simple bending due to a concentrated force at the end is given by

$$k = 3EI/l^3. \tag{7}$$

A hollow beam has cross-sectional moment of inertia given by the difference in moments of inertia between a solid beam and a beam smaller by the wall thickness. Hollow beams with an equilateral triangle cross-section, $1mm$ on a side, have been constructed by folding a $12.5\mu m$ stainless steel shim; the beam has an area moment of inertia $1.04 \times 10^{-15} mm^4$ and weighs $0.296mg/mm$. For the same mass, a $37.5\mu m$ thick, $1mm$ wide cantilever beam could be employed but it would only have an area moment of inertia of $4.39 \times 10^{-18} m^4$. Hence, the hollow triangular beam is approximately 240 times stiffer than the solid beam for the same mass (the triangular beam would be marginally stiffer in the orthogonal direction as well). A $5mm$ long triangular beam made from 302 stainless steel would have a stiffness of $4500N/m$. A peak load on the structure from the actuators of $100mN$ (see Section 4) would deflect the beam only $22\mu m$; thus this beam is stiff enough to be employed as links in the 4-bar frames.

Pin joints are difficult to place in a $1mm$ structure and they suffer problems with friction, wear, reinforcement, and alignment. Instead, flexures are employed to allow rotational motion between links. Early fatigue testing of steel flexures demonstrated that they would not be suitable ($12.5\mu m$ thick, $125\mu m$ long flexures last only 10^4 cycles, 2 orders of magnutude below the desired level). Polyester flexures, $6.25\mu m$ thick and $125\mu m$ long, have been tested over 10^6 cycles without failure and they satisfy the additional need for very low stiffness.

Figure 8(a) illustrates a sample template for the dual 4-bar mechanism. The stainless steel template can be photo-etched (useful for mass production) or laser-cut (useful for rapid-prototyping). The template is then folded into the structure shown in Figure 8(b).

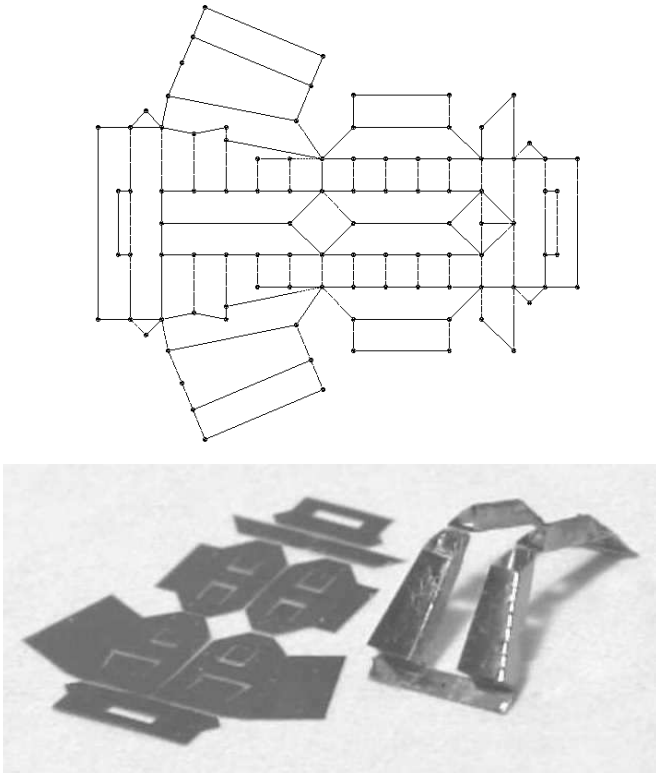

Figure 8: (a) Flat pattern for thorax dual 4-bar flexural frame and (b) photo of laser-cut sheet before and after folding.

By keeping the pair of 4-bars on the same template, alignment problems are reduced. Polyester flexures are employed at each of the joints and are glued to the flat template before folding.

Currently, the structures are folded manually using fixtures and bonded using cyanoacrylate adhesive. Automated folding of microstructures is quite feasible, particularly using simple fixtures and a motion planning approach such as that described by Lu and Akella in [13]. Tools for microassembly are described by Shimada *et al* in [19] and by Thompson and Fearing in [24].

Lightweight wings are fabricated with a polyimide spincoating step resulting in a final thickness of $7\mu m$. The wings are reinforced with $200\mu m$ diameter polyimide tubes to provide rigidity. Each wing weighs $0.5mg$ and has an inertia moment of $20mg \cdot mm^2$. Figure 9 shows the resulting wing beside the wing of a blowfly for comparison. Figure 10 illustrates a sample trajectory for the wing when it is attached to the thorax.

4 Actuation

The basic MFI actuator is the piezoelectric unimorph, illustrated in Figure 11 and described by Sitti *et al* in [21]. The beam theory for unimorph actuators is well established [22] and they have been used previously by Cox *et al* for flapping mechanisms [2]. The MFI unimorph consists of a single-crystal PZN-PT piezoelectric layer bonded to a steel elastic layer. Application of an electric field across the piezoelectric layer gives rise to longitudinal and transverse strains which lead to bending.

For a flapping mechanism with a wing load on it, design parameters such as unimorph

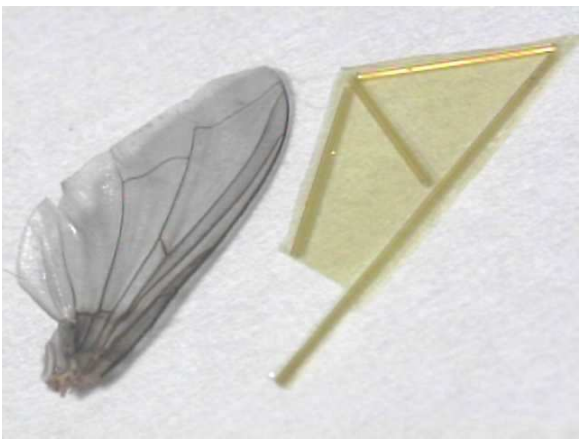

Figure 9: Photo of $0.5mg$ polyimide wing, shown with Calliphora wing for comparison.

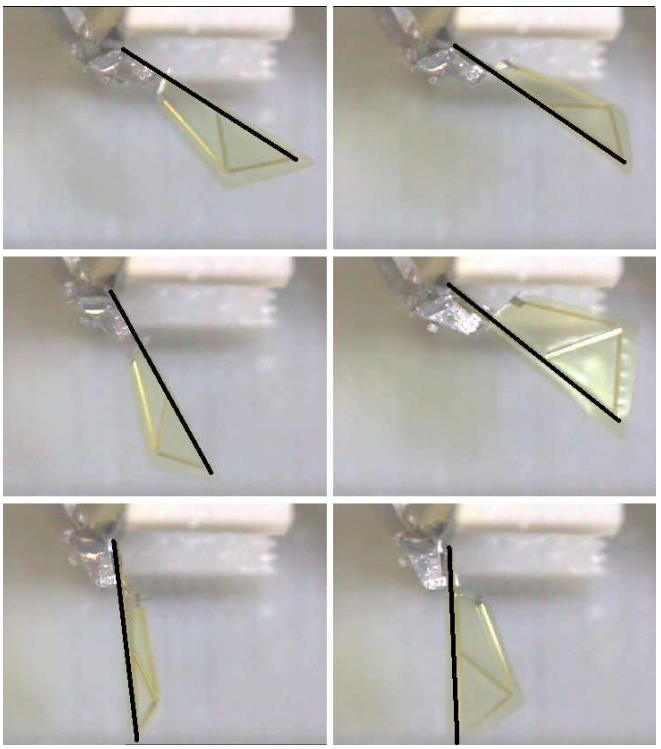

Figure 10: Clockwise sequence of images for a wing prototype driven at $100Hz$ with a rotation range of over 90° and flapping range of 80°. The dark line indicates the leading edge of the wing. The first 3 images in the sequence (starting from the top left) illustrate wing rotation at the end of a stroke.

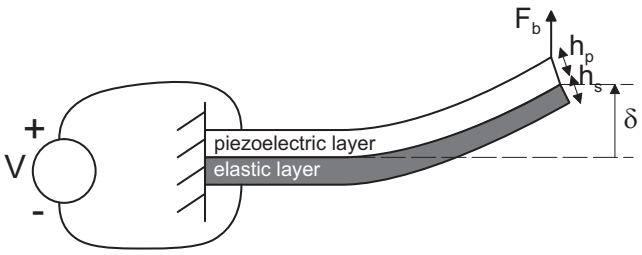

Figure 11: Basic cantilevered rectangular shape unimorph actuator structure.

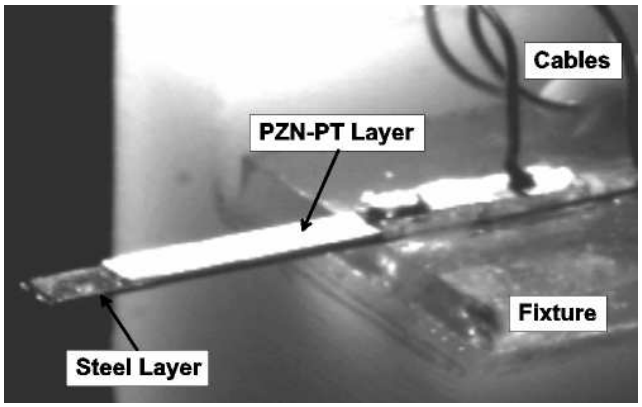

Figure 12: Photo of $5 \times 1 \times 0.22\ mm^3$ PZN-PT unimorph.

dimensions, output torque, resonant frequency, transmission ratio, quality factor, weight, *etc.* must be selected for optimal performance.

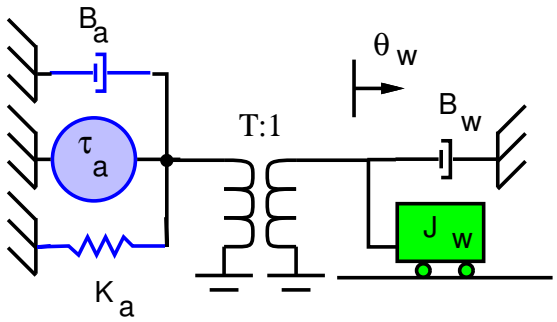

Figure 13: Linear dynamic model of piezo actuator, lossless transmission, and wing.

For simplicity, consider only the flapping degree of freedom for the following analysis. The unimorph actuator motion is amplified through the proposed thorax design described in Section 3. Consider a wing load of inertia J_w and damping B_w, and a 4-bar mechanism with stiffness K_t and stroke amplification (transmission ratio) T. A linear approximate dynamic model of Figure 13 gives:

$$J_w\ddot{\phi}_f + B_w\dot{\phi}_f + \Big(\frac{K_a}{T^2} + K_t\Big)\phi_f = \frac{\tau_a}{T} \tag{8}$$

where ϕ_f is the flapping stroke angle, K_a is the actuator rotational stiffness and τ_a is the actuator torque input. Here, the actuator damping B_a and inertia J_a are assumed to be negligible with respect to the load damping and inertia.

For a given load power requirement, the actuator dimensions are to be chosen for ease of mechanical drive, fabrication, and drive voltage requirements. Considering the

MFI specifications described in Section 1, the net wing lift force must match the insect weight of $1mN$. In the quasi-steady state, lift and drag forces are proportional to the square of velocity; however, to simplify the analysis here, a linear damper is chosen with a force at peak wing velocity equal to the MFI mass for an upper bound; this is a conservative estimate because the linear damper overestimates the damping force for all wing velocities less than the peak velocity. Hence the wing damping B_w (at the wing hinge) can be approximated as:

$$B_w \approx \frac{mgl_w}{\omega \Phi_f} = 8.65 \times 10^{-9} N \cdot s \cdot m \tag{9}$$

where $m = 100mg$, $g = 9.81m/s^2$, $l_w = 10mm$ (distance to the wing center of pressure), $\omega = 2\pi(150Hz)$, and $\Phi_f = 70^\circ$ is the wing flapping amplitude at resonance.

The quality factor Q of a resonant system is defined as the ratio of stored energy to energy dissipated per radian. With proper actuator and transmission design, energy dissipation for the MFI is work done on moving air, *i.e.*, useful work. A high Q hence implies large internal stored energy, and poor controllability of wing amplitude and phase due to actuator saturation. Sotavalta showed that blowflies have a relatively low Q, estimated on the order of 1-3 [23]. The quality factor for the thorax and wing should be about $Q_w = 2.5$, as a higher Q_w system requires a lower transmission ratio and less actuator motion at DC. A lower Q_w results in a more maneuverable wing.

The wing inertia is given by:

$$J_w = \frac{Q_w B_w}{\omega} = 2.26 \times 10^{-11} kg \cdot m^2. \tag{10}$$

The actuator stiffness, as seen at the wing hinge, must resonate at ω, hence:

$$K_1 = K_a/T^2 + K_t = J_w \omega^2 = 2.0 \times 10^{-5} N \cdot m \tag{11}$$

The four-bar transmission converts the small rotation of the actuator θ_a to the wing rotation ϕ_f by a transmission ratio T. At DC, the displacement of the wing is just:

$$\phi_{f,dc} = \frac{T\tau_a}{K_1} = \frac{2\Phi_f}{Q_w} = T\theta_{a,dc} \tag{12}$$

Then, for a given T and the desired wing flapping amplitude Φ_f at resonant frequency ω:

$$\begin{aligned} \tau_a &= \frac{2K_1\Phi_f}{TQ_w} = \frac{\phi_{f,dc}K_1}{T} \\ \theta_{a,dc} &= \frac{\phi_{f,dc}}{T} = \frac{2\Phi_f}{TQ_w} \end{aligned} \tag{13}$$

For a given h_s, h_p and V, l and w can be computed as

$$\begin{aligned} l &= \frac{h_p^2 D}{3d_{31}AB(B+1)V}\theta_{a,dc} \\ w &= \frac{4s_p}{3d_{31}h_pV}\frac{AB+1}{AB(B+1)}\tau_a \end{aligned} \tag{14}$$

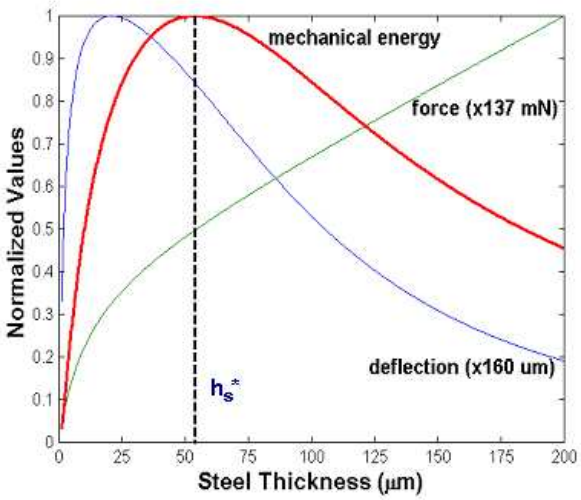

Figure 14: The effect of steel elastic layer thickness h_s on normalized values of the deflection δ_{dc}, the blocking force F_b, and the stored energy E_s for a $5mm \times 1mm$ PZN-PT unimorph with $h_p = 136\mu m$ and applied voltage of $200V$.

The average power at the wing is also another important parameter for the design which can be computed from

$$P_w = \frac{\tau_a^2 B_w}{8T^2(B_w + B_a/T^2)^2} = \frac{(mgl_w)^2 B_w}{2(B_w + B_a/T^2)^2} \tag{15}$$

where $B_a = K_a/(Q_a\omega)$, $Q_a = 20$ and $K_a = T^2(K_1 - K_t)$.

In Figure 14, the PZN-PT layer is fixed at $h_p = 127\mu m$ while h_s is varied to see how it affects the normalized values of δ_{dc}, F_b and f_r. The energy stored E_s in the unimorph reaches a maximum at $h_s^* = 53.6\mu m$. Table 3 shows the optimized E_s values for various PZN-PT unimorph thicknesses. E_s increases as h_p decreases but h_p has a minimum practical value based on the ability to polish the PZN-PT (the material is very brittle and current polishing techniques damage slabs thinner than $90\mu m$), the applied electric field (data sheets from www.trsceramics.com show crystals tested up to $120kV/cm$ so an operating voltage of $200V$ implies that $17\mu m$ is a sufficient thickness to survive), and the ultimate tensile strength of the PZN-PT.

h_p (μm)	h_s^* (μm)	E_s (μJ)
136	53.6	4.6
110	43.4	5.6
105	41.4	5.9
90	35.6	6.9

Table 3: Calculated energy storage for $5mm \times 1mm$ PZN-PT unimorph subjected to $200V$ for different h_p and h_s values.

Based on the desired Q_w, and dissipated power in a cycle, the desired E_s can be determined to be $30\mu J$. Thus, from Table III, the unimorph width can be increased to $4.3mm$ for the $90\mu m$ thick PZN-PT to give the equivalent stored energy (alternatively, the applied voltage might be increased above $400V$). Since this is the total unimorph

mass and there will be 4 actuators total, each unimorph would have dimensions $5mm \times 1.1mm \times (90\mu m$ PZN-PT $+35.6\mu m$ steel) and weigh $5mg$, as indicated in Table I.

5 Conclusion

At this stage in the MFI design, a good understanding of the necessary wing kinematics, forces, velocities and power has been developed from measurements on Robofly and real insects. Kinematic structures at the desired size scale have been fabricated using folded stainless steel to give adequate wing motion when driven by piezoelectric unimorph actuators. Polyester flexures employed at the joints between links have been tested over 10^6 cycles without failure, exceeding the original specifications. Instrumentation of the MFI with strain gauges and other sensors will permit the wing forces to be quantified. Closed-loop wing controllers are being developed to react to wing forces and modify wing stroke patterns as needed to achieve stable flight.

Acknowledgments

Thanks to K.H. Chiang, A. Majumdar, G. Moy, K. Pister, T. Sands, S. Sane and R.J. Wood for helpful discussions and insights, Jeff Thompson for laser cutting tools, Manas Menon for frame assembly and Eric Park for unimorph fabrication.

References

[1] E.A. Avallone and T. Baumeister III, editors. *Marks' Standard Handbook for Mechanical Engineers*. McGraw-Hill, 1996.

[2] A. Cox, E. Garcia, and M. Goldfarb. Actuator development for a flapping microrobotic MAV. In *SPIE Microrobotics Symp*, pages 102–8, Boston, MA, Nov 1998.

[3] M.H. Dickinson and K.G. Götz. The wake dynamics and flight forces of the fruit fly, drosophila melanogaster. *J. Exp. Biol.*, 199:2085–104, 1996.

[4] M.H. Dickinson, F-O. Lehmann, and S.P. Sane. Wing rotation and the aerodynamic basis of insect flight. *Science*, 284:1954–60, June 1999.

[5] C.P. Ellington, C. van den Berg, A.P. Willmot, and A.L.R. Thomas. Leading edge vortices in insect flight. *Nature*, 384:626–30, December 1996.

[6] R.S. Fearing, K.H. Chiang, M.H. Dickinson, D.L. Pick, M. Sitti, and J. Yan. Wing transmission for a micromechanical flying insect. In *Proc of IEEE Intl Conf on Robotics and Automation*, pages 1509–16, San Francisco, CA, April 2000.

[7] A.M. Flynn. Gnat robots and how they will change robotics. *IEEE MicroRobots and Teleoperators Workshop*, Nov 9-11 1987.

[8] R.H. Francis and J. Cohen. The flow near a wing which starts suddenly from rest and then stalls. *Rep Memo Aeronaut Res Comm*, 1561, 1933.

[9] H. Hosaka, K. Itao, and S. Kuroda. Evaluation of energy dissipation mechanism in vibrational microactuators. In *IEEE Micro Electro Mechanical Systems*, pages 193–8, Oiso, Japan, Jan 25-28 1994.

[10] M. Jensen and T. Weis-Fogh. Biology and physics of locust flight. v. strength and elasticity of locust cuticle. *Philos. Trans.*, 245(B. 721):137–69, 1962.

[11] C. Keller. *Microfabricated High Aspect Ratio Silicon Flexures.* MEMS Precision Instruments, El Cerrito, CA, 1998.

[12] Y. Kubo, I. Shimoyama, T. Kaneda, and H. Miura. Study on wings of flying microrobots. In *Proc of IEEE Intl Conf on Robotics and Automation*, pages 834–9, San Diego, CA, May 1994.

[13] L. Lu and S. Akella. Folding cartons with fixtures: A motion planning approach. In *Proc of IEEE Intl Conf on Robotics and Automation*, pages 1570–6, Detroit, MI, May 1999.

[14] M.L. May. Dragonfly flight: Power requirements at high speed and acceleration. *J. Exp. Biol.*, 158:325–42, 1991.

[15] J.M. McCarthy. *Geometric Design of Linkages.* Springer-Verlag, 2000.

[16] N. Miki and I. Shimoyama. Analysis of the flight performance of small magnetic rotating wings for use in microbots. In *Proc of IEEE Intl Conf on Robotics and Automation*, pages 3065–70, Leuven, Belgium, May 1998.

[17] W. Nachtigall, A. Wisser, and D. Eisinger. Flight of the honey bee. VIII. functional elements and mechanics of the 'flight motor' and the wing joint - one of the most complicated gear-mechanisms in the animal kingdom. *J. Comp. Physiology B*, 168:323–44, 1998.

[18] L. Schenato, X. Deng, and S. Sastry. Virtual insect flight simulator (VIFS): A software testbed for insect flight,. In *Proc of IEEE Intl Conf on Robotics and Automation*, pages 3885–92, Seoul, Korea, May 21-26 2001.

[19] E. Shimada, J.A. Thompson, J. Yan, R.J. Wood, and R.S. Fearing. Prototyping millirobots using dextrous microassembly and folding. In *Symp on Microrobotics ASME Intl Mech Eng Cong and Expo*, Orlando, FL, Nov 5-10 2000.

[20] I. Shimoyama, H. Miura, K. Suzuki, and Y. Ezura. Insect-like microrobots with external skeletons. *IEEE Control Systems Magazine*, 13:37–41, February 1993.

[21] M. Sitti, D. Campolo, J. Yan, R.S. Fearing, T. Su, D. Taylor, and T.D. Sands. Development of PZT and PZN-PT based unimorph actuators for micromechanical flapping mechanisms. In *Proc of IEEE Intl Conf on Robotics and Automation*, pages 3839–46, Seoul, Korea, May 21-26 2001.

[22] J. Smits and W. Choi. The constituent equations of piezoelectric heterogenous bimorphs. *IEEE Tran. on Ultrasonics, Ferroelectrics, and Freq Control*, 38:256–70, May 1991.

[23] O. Sotavalta. The wing stroke frequency of insects in wing mutilation and loading experiments at sub-atmospheric pressure. *Ann. Zool. Soc.*, 15(2):1–67, 1952.

[24] J.A. Thompson and R.S. Fearing. Automating microassembly with ortho-tweezers and force sensing. In *to appear, IROS 2001*, Maui, HI, Oct 29-Nov 3 2001.

[25] J. Yan, R.J. Wood, S. Avadhanula, M. Sitti, and R.S. Fearing. Towards flapping wing control for a micromechanical flying insect. In *Proc of IEEE Intl Conf on Robotics and Automation*, pages 3901–8, Seoul, Korea, May 21-26 2001.

[26] R. Yeh, E.J. Kruglick, M. Klitzke, and K.S.J. Pister. Towards an articulated silicon microrobot. In *Winter Annual Meeting, ASME*, Dec 1994.